npj | flexible electronics

Article

Published in partnership with Nanjing Tech University

https://doi.org/10.1038/s41528-025-00390-y

# Stretchable optoelectronic synapses with ultraviolet to near-infrared perception for retina-inspired computing and vision-adaptive sensing



Linfeng Lan[1] ✉, Bo Huang[1], Yaping Li[1], Churou Wang[1], Jiayi Pan[1], Jiale Huang[1], Baozhong Chen[1], Qi zhou[1], Longzhen Qiu[2] ✉, Yafei Ding[3], Qing Wan[4], Zhong Ji[5], Yuan Li[1], Junbiao Peng[1] ✉ & Yong Cao[1]

Stretchable optoelectronic synapses are attractive for intelligent perception, neuromorphic computation and visual adaptation. Here, we demonstrate a highly stretchable organic optoelectronic synaptic transistor (s-OOST) with a transconductance up to 86 mS that can simultaneously accept modulation of electrical pulses and multi-wavelength light signals (from ultraviolet to near-infrared). The s-OOST achieved highly reliable synaptic plasticity for brain-inspired computation and retina-inspired perception even under 50% tensile strain. Furthermore, the devices exibited vision-adaptive near-infrared sensing ability that was verified by single-pixel scanning imaging. Finally, the multi-wavelength (365 nm–1050 nm) optical synaptic properties were investigated under the applications of imaging memory, polychromatic optical communication and information security (coded by wavelength). This research advances the capabilities of the stretchable integrated systems with vision-adaptive sensing characteristic and computing-in-memory ability.

Synaptic transistors (STs) that can memorize and process signals in a single device have drawn extensive attention for potential applications in next-generation artificial intelligence (AI) based on brain-inspired neuromorphic computation. The high-efficient in-memory computing (IMC) and learning abilities make the ST be one of the hotspots of current research. As a special kind of STs, the optoelectronic synapse transistors (OST) that can perceive, process and memorize both electrical and optical signals is particularly attractive[1–3], because it has additional abilities of visual perception and/or visual self-adaptation/regulation similar to the human retina. However, the reported OSTs generally exhibit monotonous functionality and poor biocompatibility (unstretchable/undeformable), which cannot perform complex tasks in dynamic/unstructured environments such as in wearable and implantable electronics[4,5]. Therefore, stretchable/deformable OSTs are extremely desirable for the vision-inspired neuromorphic systems with free deformation and cross-scale modulus adaptability[6,7]. Compared to the structurally stretchable design, the intrinsically stretchable design enables more convenient fabrication, higher versatility and availability, becoming an inevitable componence for next-generation human-oriented applications[8]. Notably, intrinsically stretchable synaptic devices based on organic semiconductors are particularly appropriate for the purpose of emulating the functions of living systems owing to their mechanical compliance, biocompatibility and excellent optoelectronic properties[1,3,8–19]. However, relatively fewer works have been carried out on stretchable organic optoelectronic synaptic transistor (s-OOSTs) based on inherently stretchable materials featuring both highly reliable electrical synaptic plasticity and multi-wavelength (broadband) vision-inspired neuromorphic response. Most of stretchable photosensitive organic semiconductors typically have a narrow absorption range or limited mechanical ductility. Tae-Woo Lee et al. constructed a stretchable organic nanowire synaptic transistor (s-ONWST) with a semiconductor of FT4-DPP-based polymer, but external photoreceptors are required to convert the external optical signals to electrical signals, which increases the complexity and reduces the efficiency[17].

In this paper, a broadband (365–1050 nm) responsive s-OOST based on intrinsically stretchable, high-mobility, narrow-bandgap, high-relaxation-time organic semiconductor was constructed to achieve brain-inspired memory/computation and retina-inspired visual

[1]Guangdong Basic Research Center of Excellence for Energy and Information Polymer Materials, State Key Laboratory of Luminescent Materials and Devices, South China University of Technology, Guangzhou, China. [2]School of Instrument Science and Opto-Electronic Engineering, Hefei University of Technology, Hefei, China. [3]Southern University of Science and Technology, Shenzhen, China. [4]Yongjiang Laboratory, Ningbo, China. [5]Guangzhou Institute of Technology, Xidian University, Guangzhou, China. ✉e-mail: lanlinfeng@scut.edu.cn; lzhqiu@hfut.edu.cn; psjbpeng@scut.edu.cn

perception/adaptation. The s-OOSTs exhibited high transconductance (86 mS, highest in synapses) at a low voltage (−1 V) and could stand against 50% multidirectional strain. When stimulated by the gate pulse, the postsynaptic current (PSC) of the s-OOSTs exhibited neuromorphic behaviors, such as conversion from short-term plasticity (STP) to long-term plasticity (LTP), spike duration-dependent plasticity (SDDP), pair pulse facilitation (PPF, as high as 264%), spike number-dependent plasticity (SNDP) as well as "learning-forgetting-relearning" behaviors (with a high recognition accuracy of 88.75% simulated by handwritten digital datasets). Furthermore, the s-OOSTs can be stimulated by the light from ultraviolet (UV) to near-infrared (NIR) (365 nm–1050 nm), which is the widest wavelength response ever report. The relaxation time of the s-OOSTs changes greatly with the wavelengths of the incident light, making the devices possess additional abilities of light plasticity, color identification and visual self-adaptation similar to human retina. Moreover, the synaptic performance was investigated at low temperature and vacuum condition. The broadband spectrum response makes it successfully image the letters "SU" in NIR environment with high contrast ratio in a single-pixel scanning imaging system, which verifies the feasibility for near-infrared imaging and visual response of the single s-OOST devices. Finally, multi-wavelength (365nm-1050 nm) optical synaptic plasticity was investigated for the imaging memory, polychromatic optical communication and information security. A series of "bus" images and letters (coded by wavelength) with different colors were identified and memorized by the s-OOSTs. This research promotes the development of the intrinsically stretchable optoelectronic transistors with broadband response from UV nm to NIR.

## Results

### Device design philosophy and electrical characteristics

Figure 1a–c show fabrication scheme and electrical properties of the s-OOSTs. The detailed fabrication process is described in Methods section. Step I. and II. in Fig. 1a show the fabrication process of the dextran/TPU films, the schematic structure of the s-OOST and the molecular formulas of the organic semiconductor and the ionic gel. Dextran is a hydrophilic material suitable for peeling off the hydrophobic thermoplastic polyurethane (TPU) film from the wafers[20]. TPU is a transparent, elastic polyurethane material with excellent film forming ability and high stretchability, which meets the demand of smooth and dense substrate for the organic semiconducting films[21,22]. The organic semiconductor—Poly-diketo-pyrrolopyrrole-selenophene-*x* hybrid siloxane-based side chains (PTDPPSe-*x*Si, $x = 3–7$)) —is an intrinsically stretchable a donor-acceptor (D-A) material[23]. Specifically, the PTDPPSe main chain has narrow bandgap and excellent charge transport properties. A certain length of the hybrid siloxane-based side chains ($x = 6$ in this paper, that is, PTDPPSe-6Si) was grafted onto the polymer main chain to enhance its stretchability. The PTDPPSe-6Si has the advantages of high mobility (>1 $cm^2$/Vs), high stretchability (≥100%), narrow gap (1.50 eV), long relaxation time and high photoelectric conversion efficiency, which is extremely attractive in the field of optoelectronic synaptic devices.

The multi-wall carbon nanotubes (MWCNTs) electrodes were deposited by spraying process (Fig. 1b)[24]. Then, an ionic gel film was laminated onto the channel[25]. After that, the device was immersed in deionized water to remove the dextran sacrificial layer so as to peel off the s-OOST from the substrate (Fig. 1c). Supplementary Fig. 1a–c show the

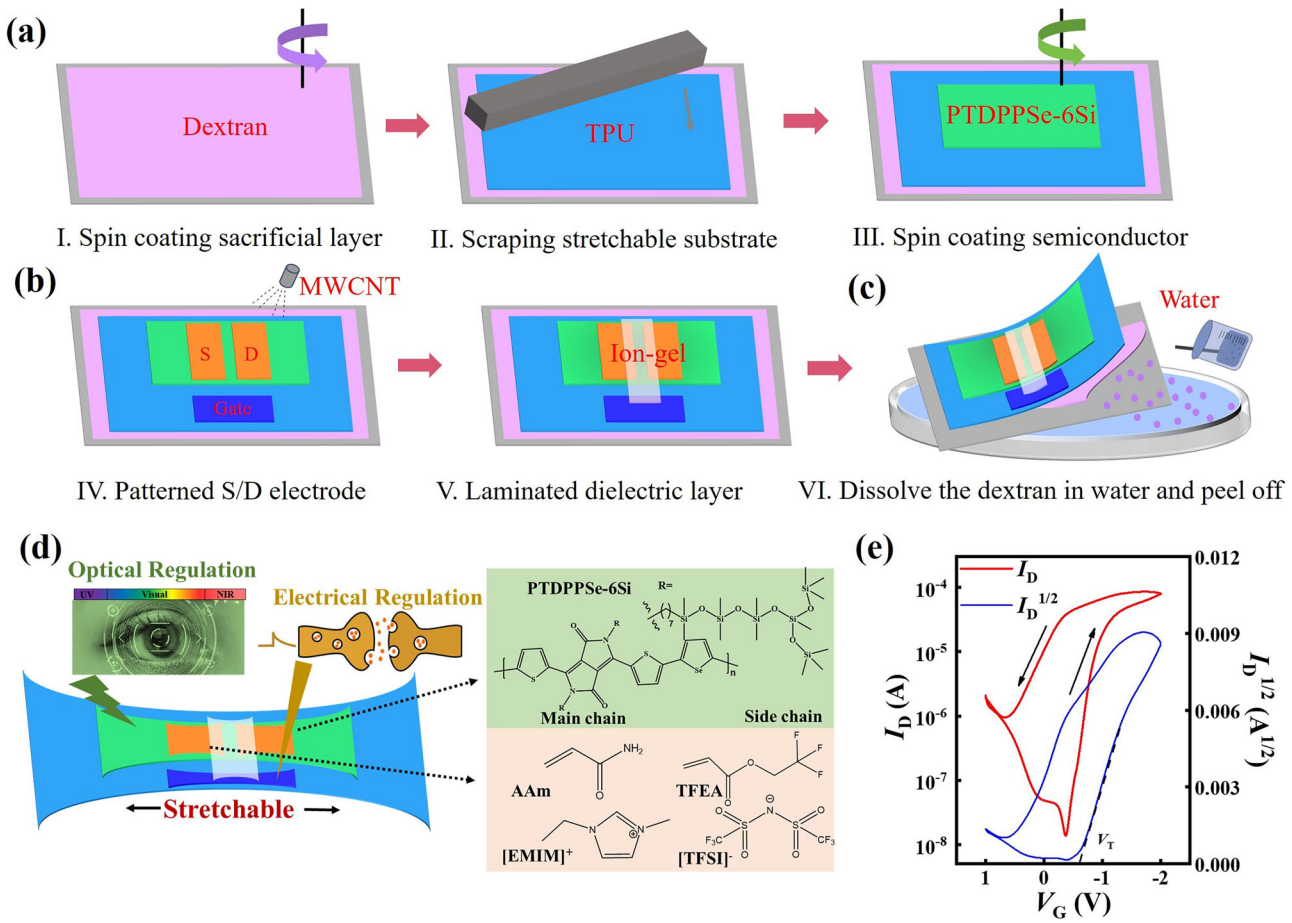


**Fig. 1 | Fabrication scheme and electrical properties of the s-OOSTs.** **a** Preparation of dextran/TPU/PTDPPSe-6Si. **b** Preparation of stretchable SWCNT source/drain (S/D) and gate electrodes/stretchable ion gels. **c** Removing the water-soluble sacrifice layer to get an intelligent sensing/optoelectronic integrated organic stretchable synapse. **d** Schematic structure of the s-OOSTs and the molecular formulas of the organic semiconductor and ionic gel. **e** Transfer curves of the s-OOSTs.

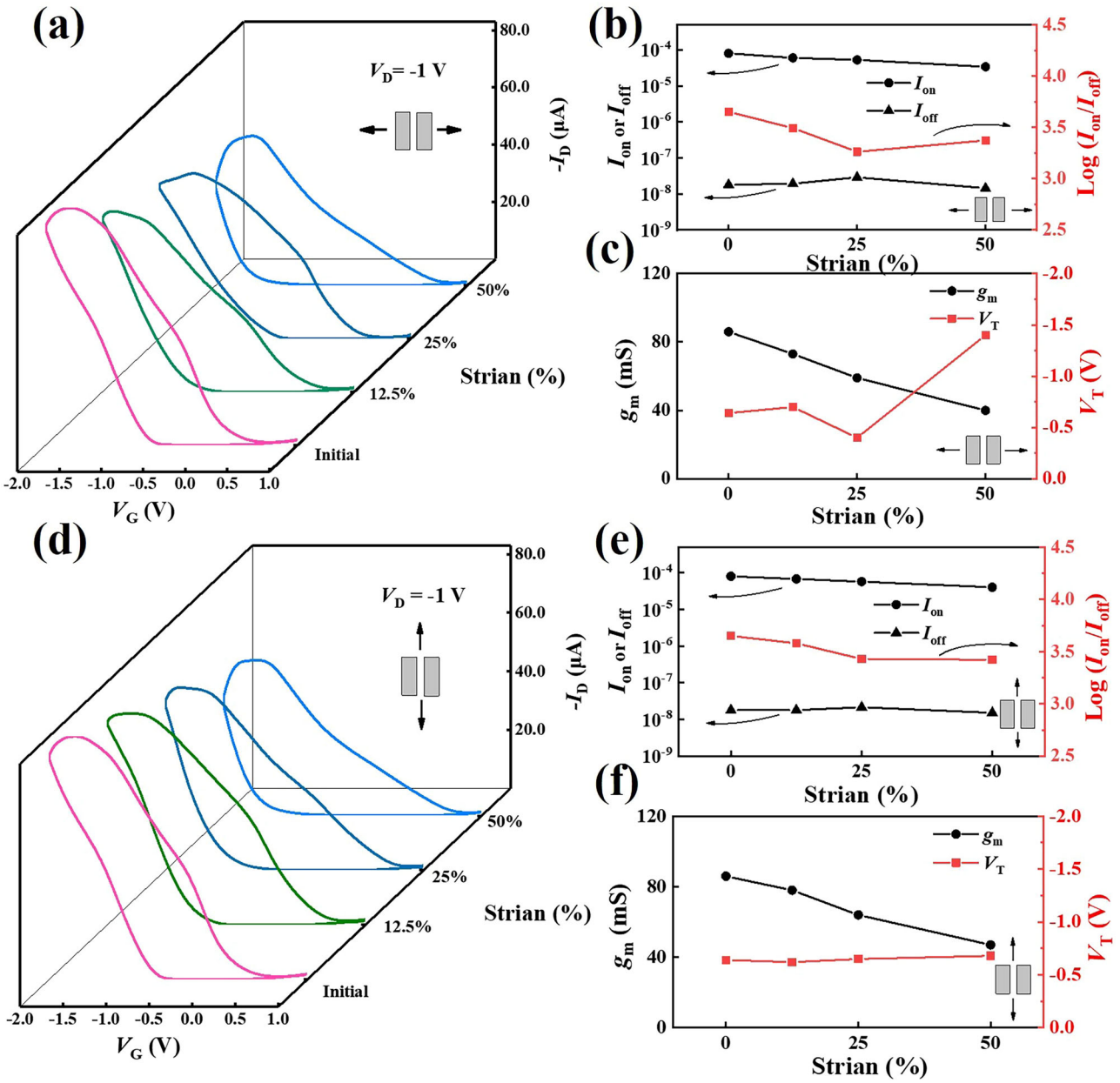


**Fig. 2 | Electrical/mechanical performance of the s-OOSTs. a** Transfer curves of the s-OOSTs under parallel strains. **b** $I_{on}$, $I_{off}$ and Log ($I_{on}$/$I_{off}$) of the s-OOSTs under parallel strains. **c** $g_m$ and $V_T$ of the s-OOSTs under parallel strains. **d** Transfer curves of the s-OOSTs under vertical stains. e $I_{on}$, $I_{off}$ and Log ($I_{on}$/$I_{off}$) of the s-OOSTs under vertical strains. **f** $g_m$ and $V_T$ of the s-OOSTs under parallel strains.

scanning electron microscope (SEM) images of the TPU, PTDPPSe-6Si and MWCNT, respectively. The surface of the TPU substrate was smooth, and the PTDPPSe-6Si film covered well onto the TPU substrate without any cracks. The MWCNTs were seen clearly in the inset of Supplementary Fig. 1c. Figure 1d shows the schematic structure of the s-OOST and the molecular formulas of the organic semiconductor and the ionic gel. Figure 1e shows the transfer curves of the s-OOSTs. The drain current ($I_D$) was obtained by sweeping the gate voltage ($V_G$) from 1 to −2 V and then back to 1 V while the drain voltage ($V_D$) was kept at −1 V. The s-OOSTs exhibited large hysteresis that is essential for mimicking the biological synapses that have plasticity ability. The on/off current ratio ($I_{on}$/$I_{off}$, switching ability) was ~$10^4$, and the threshold voltage ($V_T$) obtained by $I_D^{1/2}$ ~ $V_G$ curve fitting was −0.64 V, which means that the s-OOST is enhancement-mode transistors[18]. Owing to the high mobility of the PTDPPSe-6Si organic semiconductor, a transconductance of as high as 86 mS were attained for the s-OOST (Supplementary Fig. 1d), which is comparable to those of the best organic synaptic transistors ever reported (Supplementary Table 1)[12,17,26–36]. Supplementary Fig. 2 shows the transfer curves of the s-OOST under repeated forward/reverse sweeps. The device exhibited relatively good repeatability.

### Intrinsic stretchability

Figure 2a shows the transfer curves of the s-OOSTs under different levels of mechanical strain along (parallel) to the channel (carrier transport) directions. The $I_D$ (at $V_G$ = −2 V) of the unstretched s-OOST was ~80 μA. After parallelly stretched for 12.5%, 25% and 50%, the $I_D$ decreased to 59, 53 and 34 μA, respectively. The on/off current ratios ($I_{on}$/$I_{off}$) and the $g_m$/$V_T$ of the s-OOSTs under different parallel strains are plotted in Fig. 2b, c, respectively. When the s-OOSTs were vertically stretched for 12.5%, 25% and 50%, the $I_D$ decreased to 69, 57, and 41 μA, respectively (decreased more slowly compared to the parallelly stretched one). Figure 2d shows the transfer curves of the s-OOSTs under different levels of mechanical strain perpendicular (vertical) to the channel directions. The $I_{on}$/$I_{off}$ and the $g_m$/$V_T$ of the

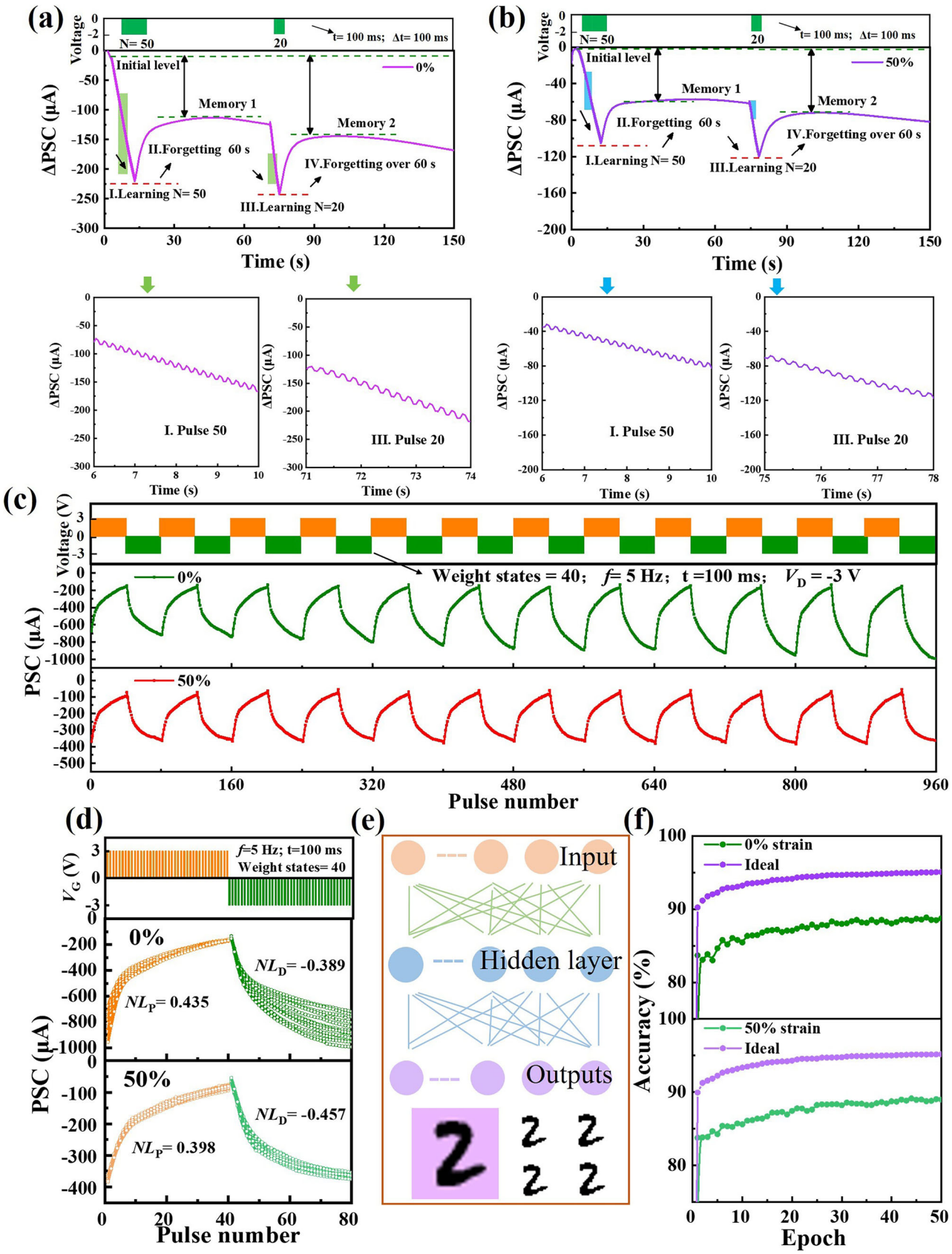


**Fig. 3 | Brain-inspired behaviors and neural morphology simulation of the s-OOSTs under electrical pulse stimulation. a** Learning-forgetting-relearning" brain-inspired behaviors under 0% strain. **b** "Learning-forgetting-relearning" brain-inspired behaviors under 50% strain. **c** ΔPSC under successive positive-negative pulse groups. **d** Average *NL* value at different strains. **e** MNIST dataset and neural network with three layers of ANN. **f** The recognition accuracy of 28 × 28 pixel handwritten digital images with training epochs measured at 0% and 50% strains.

s-OOSTs under different vertical strains are plotted in Figs. 2e and 2f, respectively. The decrease in $I_{on}$ and $g_m$ under vertical strains was less than those under parallel strains, because the vertical stretching increases the channel width ($W$), while does not change length ($L$), resulting in an increase in $W/L$ and a smaller attenuation in $I_{on}$ and $g_m$. Supplementary Fig. 3 shows the leakage current of the static strain, the leakage current were about 0.41 μA (0%), 0.38 μA (12.5%), 0.20 μA (25%) and 0.4 μA (50%) under parallelly stretching, and 0.41 μA (0%), 0.44 μA (12.5%), 0.41 μA (25%) and 0.36 μA (50%) under vertically stretching. It shows that the EMIM-TFSI ion-gel dielectric layer is able to withstand 50% stain without significant changes in the leakage current. Supplementary Fig. 4a shows the tensile durability of the s-OOSTs under 500 repeated stretch/release cycles (50% parallel strain). After 500 stretch/release cycles, the $I_{on}$ decreased from ~80 μA to ~50 μA) while the $I_{off}$ did not changed much (around 15–20 nA under different strain cycles), resulting a slight decrease in the on/off ratio (Supplementary Fig. 4b). The leakage of the dynamic strain is shown in Supplementary Fig. 4c. It reveals that the s-OOSTs are able to withstand 500 stretch/release cycles. The comparison of the static and dynamic strain of the s-OOSTs with the devices reported before is summarized in Supplementary Table 2.

### Synaptic behaviour regulated by electrical pulses

Supplementary Fig. 5a shows the schematic transmission principle of the neural system. A biological synapse is a structure that transmits neural information from one neuron to the next in the form of serial propagating action potentials. This process can be simulated by the s-OOSTs. Supplementary Fig. 5b shows the working principle of the s-OOSTs that emulates biological synaptic functions. When a pulse signal is applied to the gate, the channel current between source and drain changes, corresponding to ΔPSC (the changes of the postsynaptic current), which can be modulated by a series of factors such as pulse width. The ΔPSC reflects the variations in synaptic weights that represent connection strength between two synaptic neurons and associate with the learning and memory processes in human brains. The synaptic plasticity can be mainly separated into STP and LTP according to the duration to assess memory characteristics.

To characterize the SDDP of the s-OOSTs, presynaptic pulse signals with different pulse widths ranging from 50 to 1000 ms were applied to the gate. Supplementary Fig. 5c depicts the ΔPSC after applying pulse signals to the gate of the s-OOSTs. The ΔPSC increased from 14 to 108 μA when the pulse width increased from 50 to 1000 ms. When stretched by 50%, the s-OOSTs maintained good SDDP with ΔPSC increased from 3 (50 ms) to 32 μA (1000 ms). The SDDP behavior is due to the increase in the number of ions accumulated at the ion gel/channel interface with an increasing pulse width (the ions have more time to move to the interface). The response current (*ReC*) and the memory current (*MeC*) are defined as Eqs. (1) and (2), respectively[1].

$$Response\ current(ReC) = \left|I_1 - I_0\right| \tag{1}$$

$$Memory\ current(MeC) = \left|I_2 - I_0\right| \tag{2}$$

Where $I_0$ represents the initial ΔPSC before triggering; $I_1$ indicates the peak ΔPSC during triggering; and $I_2$ indicates ΔPSC for 1 s after triggering. The s-OOSTs showed increasing memory level (the *MeC* increased from 7 to 63 μA) with an increasing pulse width (from 50 to 1000 ms). The plasticity transferred from STP to LTP (if defining $MeC > 15$ μA for LTP) when the pulse width reached 200 ms.

PPF is a typical form of STP, which is defined as the ratio of the height of the second peak ΔPSC ($A_2$) to the height of the first peak ΔPSC ($A_1$) under the stimulation of two consecutive $V_G$ pulses with the same shape. The PPF index is defined as[18]

$$PPF\ index = \frac{A_2}{A_1} \times 100\% \tag{3}$$

The PPF index is greater than 100%, because some of the induced ions in the first pulse still exist at the ion gel/channel interface, resulting in a higher conductance in the second pulse. Supplementary Fig. 5d shows the ΔPSCs of the s-OOST triggered by two successive presynaptic pulses with a $\Delta t$ of 1000 ms. A PPF index of 185% was obtained for the unstretched s-OOSTs under electrical pulse simulation. After stretched by 50%, the PPF index was 167%. The PPF index can be strengthened by adjusting the interval between the two successive pulses. Supplementary Fig. 6 shows the ΔPSCs of the s-OOSTs triggered by two successive presynaptic pulses with different $\Delta t$. The lower PPF for longer $\Delta t$ is due to the relaxation of the ions. Upon stretching by 50%, the PPF index did not changed much. Energy efficiency is necessary for neuromorphic computation. When stimulated by a single $V_G$ pulse (−30 mV, 10 ms), the PSC signal (with an amplitude of 3.7 pA) remained clearly detectable even at a $V_D$ of −100 μV. According to Eq. (4)[10]

$$W = V_D \times I_D \times t \tag{4}$$

the minimum energy consumption of the single-event operation of the s-OOSTs was 3.7 aJ (Supplementary Fig. 7). The signal to noise ratio (S/N) is also shown in Supplementary Fig. 7. The SNR of the PSC signal is determined by the Eq. (5)[37]

$$SNR = 10\lg\left(\frac{S}{N}\right) \approx 10\lg\left(\frac{PSC}{Noise}\right) \tag{5}$$

The S/N was calculated to be 18.5, 33.5 and 68, corresponding to the pulse width of 10 ms, 20 ms and 50 ms, respectively. For neuromorphic engineering applications, both high SNR and low energy consumption are needed. The corresponding SNR was calculated by Eq. (5) to be 12.68 dB, 15.25 dB and 18.30 dB, and the corresponding energy consumption was 3.7 aJ, 13.4 aJ and 224 aJ, respectively. The summarized S/N and SNR value are shown in Supplementary Table 3 [37–42]. The S/N and SNR value were relatively high even at $V_D = -100$ μV in a relative energy-efficient state.

The response and memory level of the s-OOSTs also increased with an increasing pulse number (N). Supplementary Fig. 8 shows the ΔPSCs of the s-OOSTs when applying pulse signals with different pulse number of 5–50 to the gate of the s-OOSTs. ΔPSCs increased as the pulse number increased. As the pulse number increased from 5 to 50, the *ReC* increased from 83 to 227 μA (Supplementary Fig. 9a), and *MeC* strengthened from 31 μA to 147 μA (Supplementary Fig. 9b). Similar results were found under 50% strain.

### Brain-inspired computation

"Learning-forgetting-relearning" behavior is a critical indicator for the learning and memory ability of human brains. As shown in Fig. 3a, after a period of learning by applying 50 successive $V_G$ pulses, the ΔPSC increased to a peak value and then decreased slowly, which is similar to repetitive learning behavior of human brain. After 60 s forgetting, the ΔPSC was still much larger than the initial ΔPSC. It reflects that the s-OOSTs has excellent memory ability. After the second learning period with much fewer pulses (20 successive pulses), the s-OOSTs reached a higher ΔPSC than that after the first period of learning strength, indicating that the s-OOSTs have certain associating and relearning ability. Moreover, after the second learning period, the forgetting time increased to >>60 s. This indicates that the s-OOSTs can reduce the learning time and increase the memory time through training. Similar results can be found under 50% strain (Fig. 3b). The result shows that the s-OOSTs have great potential for deep learning ability.

Figure 3c shows the potentiation and depression (PD) response of the s-OOSTs under 12 PD cycles (each cycle included 40 pulses of +3 V and 40 pulses of −3 V in series, the frequency was 5 Hz, $\Delta t$ = 100 ms). In each cycle, the PSC changed from about −800 μA to about −169 μA after 40 potentiation pulses and then changed to about −890 μA after 40 depression pulses, reflecting good cycling stability with multiple PD pulse sets. To

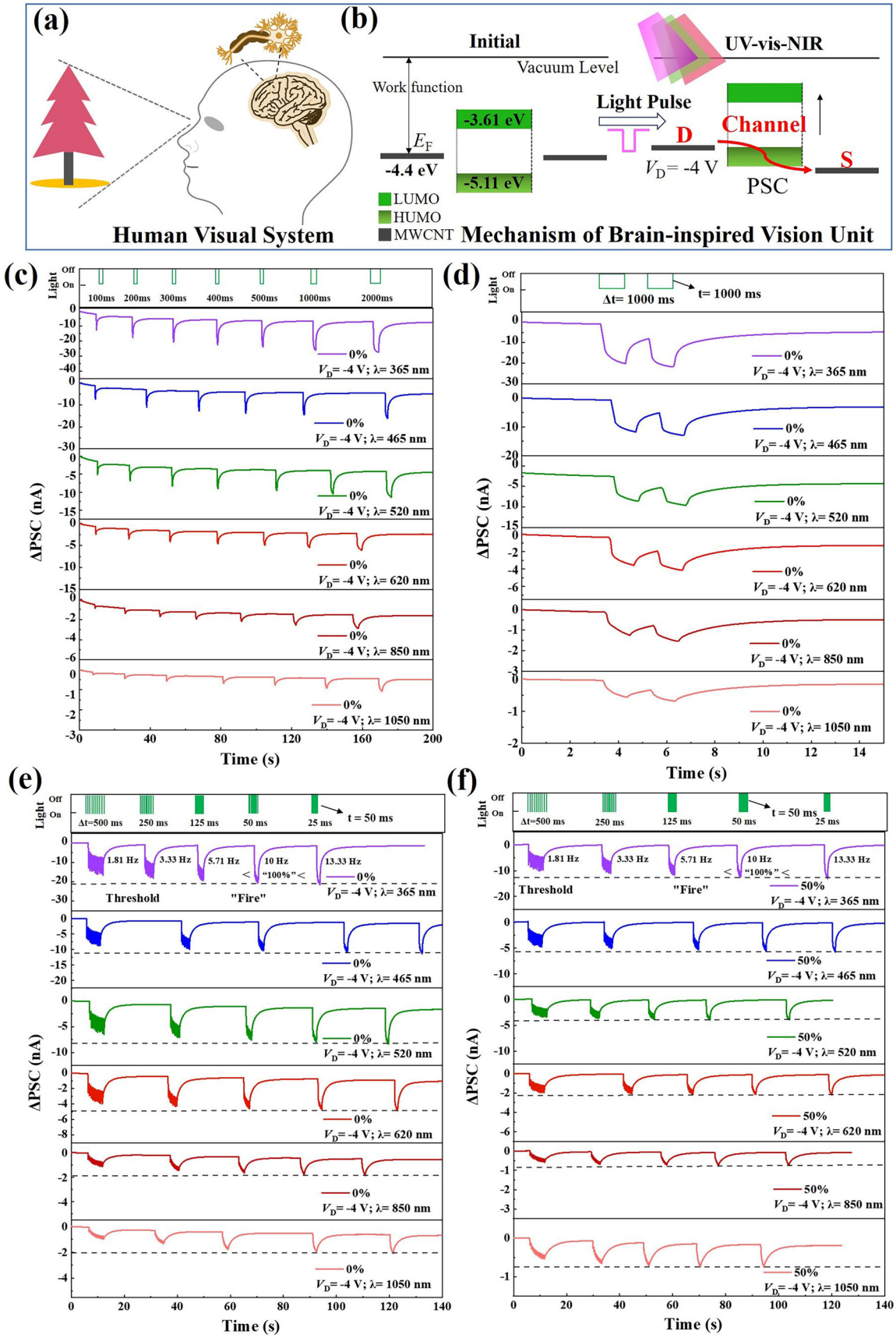


**Fig. 4 | Principle of photo synapse and synaptic performance under photo stimulation of the s-OOST. a** Schematic structure of human visual system. **b** Schematic diagram of the s-OOSTs triggered by different light from UV to NIR. **c** Synaptic plasticity of s-OOST stimulated by single pulse with different pulse widths **d** Synaptic plasticity of s-OOST stimulated by two successive pulses with $\Delta t$ = 1000 ms. **e** The filter effect at 0% strain. **f** The filter effect at 50% strain.

investigate the PD linearity of the s-OOSTs, the nonlinearity (*NL*) is introduced, which can be expressed as Eq. (6) [43].

$$NL_{P,D} = average\left(\frac{Max|I_{P,D}(n) - I_{Linear}(n)|}{I_{P,D}(40) - I_{P,D}(1)}\right), \text{For n} = 1 \text{ to } 40 \quad (6)$$

Where $I_P$ and $I_D$ are actual potentiation and depression of the synaptic current, respectively; and $I_{Linear}$ is the ideal linear current. Lower *NL* represents better linearity. As depicted in Fig. 3d, The $NL_P$ was 0.435 and and the $NL_D$ was −0.389 for the unstretched s-OOSTs. Upon stretching by 50%, the $NL_P$ and $NL_D$ were calculated to be 0.398 and −0.457, respectively. The result reflects that the s-OOSTs have good linearity, uniformity, and repeatability even under 50% strain.

The s-OOSTs were used for image recognition by using MNIST dataset to simulate a neural network in recognition tasks. Figure 3e shows the schematic diagram of a representative MNIST hand written digit "2" and a neural network composed of s-OOSTs. The fully connected layers include 784 input neurons, 200 hidden neurons, and 10 output neurons, and the backpropagation algorithm was used for training. The s-OOST was a unit of the array of the synaptic weight layers whose channel conduction changes were considered as weight updates for executing backpropagation algorithms. The cumulative distribution function (CDF) of each conductivity state was recorded to illustrate the device noise, nonlinearity, and asymmetry in the algorithm. CDF is expressed as[44]:

$$CDF_G(\Delta G_x) = \int_{(\Delta G)_{min}}^{\Delta G_x} \rho_G(\Delta G) dG_x \quad (7)$$

where $\rho_G$ ($\Delta G$) is the probability distribution under a certain conductance state as shown in Supplementary Fig. 10. A large image of handwritten digits (28 × 28 pixels) from the MNIST dataset was utilized for the simulation. After 40 training cycles, as shown in Fig. 3f, the recognition accuracy reached 88.7% (0% strain) and 88.9% (50% strain), indicating that the s-OOSTs have potential in applications in brain-inspired computing.

### Visual synaptic behaviours regulated by UV-visible-NIR light

Traditionally, artificial vision system consists of optical sensors, data memories and signal processing modules for image recognizing and processing[1,18]. In the system, the optical sensors sense the external optical signals and convert them to electrical signals before delivery to the memories for storage, and then the signals are processed by the signal processing modules to complete the image processing and classification tasks, causing high latency for data transmission and high power consumption for the overall system. In contrast, in human visual system (Fig. 4a), retinal neurons not only detect light signal but also preprocess visual signals, so the subsequent recognition and decision-making tasks can be done more efficiently and accurately[45,46]. Here, the s-OOSTs may have the ability of processing light signals efficiently as the human visual system because of the broadband light sensitivity and long relaxation time of the PTDPPSe-6Si semiconductor. The working mechanism of the s-OOST brain-inspired vision system is illustrated in Fig. 4b. The UV-vis-NIR absorption spectra of the PTDPPSe-6Si semiconductor is shown in Supplementary Fig. 11a. The absorption spectra of the PTDPPSe-6Si semiconductor exhibited two typical absorption bands, one for intramolecular charge transfer (ICT, 600 − 1000 nm) between the donor (D) and aceptor (A) conponents, and the other for $\pi - \pi^*$ transitions (300 − 600 nm), and the two absorption bands "0-0" and "0-1" in Supplementary Fig. 11a were corresponding to the absorption of the aggregated and nonaggregated state. The absorption spectrum can be expressed as

$$a(\hbar w) = \sum_{\{v_i\}} a_0(\hbar w - \sum v_i \hbar w_i) \prod_i |\langle \chi(v_i)|\chi(0)\rangle|^2 \quad (8)$$

where $a$ ($\hbar w$) is the absorption coefficient; $\hbar w_i$ is the interval between vibrator levels; $v_i$ is the number of phonons in the excited state. The zero order expression of Eq. (6) can be derived as:

$$a_0(\hbar w) = \frac{1}{(\hbar w)^2} \int \frac{e^{-(\Delta - \Delta_0)2/\gamma^2}}{\sqrt{(\hbar w)^2 - 4\Delta^2}} d\Delta \quad (9)$$

$a_0$ ($\hbar w$) represents the fitting results of the absorption of spectrum curve; $\gamma$ is the width residual disorder; and $\Delta_0$ is recombination energy (the band gap $E_G = 2\Delta_0$). The detailed description and derivation process of the zero order absorption equation are disscussed in Supplementary Note 1 and Supplementary Note 1 Fig. 1 of the Supplementary Information. The fitting parameters of the curve: $\Delta_0 = 0.71$ eV (indicating that the PTDPPSe-6Si has excellent emission properties), and $\gamma = 0.08$ (indicating that the Gaussian distribution width is narrow and the excitation probability varies greatly at different wavelengths, see Supplementary Fig. 11b). Supplementary Fig. 11c shows the photoluminescence spectrum (PL) excited by an 808 nm light source. Dual emission peaks at 948 nm (1.31 eV) and 1040 nm (1.19 eV) were observed, which present wide and high emission bands "0—0" and "0—1". Due to the excellent optoelectronic conversion effect of PTDPPSe-6Si with a narrow band gap ($E_G = 1.50$ eV, near the fitting result, $E_G = 2\Delta_0 = 1.42$ eV), the s-OOSTs were able to generate corresponding PSC by absorbing light with wavelength ranging from UV to NIR light. Supplementary Fig. 12 shows the NIR/fluorescence lifetime of the charge carriers the PTDPPSe-6Si semiconductor excited by different light wavelengths (ex808 nm and 375nm-EPL). The result can be fit by Eq. (10) [1]

$$R(t) = A_1 \exp(-t/\tau_1) + A_2 \exp(-t/\tau_2) + A_3 \exp(-t/\tau_3) \quad (10)$$

where $\tau_1$, $\tau_2$ and $\tau_3$ are lifetime parameters, respectively; $A_1$, $A_2$ and $A_3$ are proportional constants. The fitting results are listed in Supplementary Table 4. It is interesting that the lifetimes excited by 808 nm (μs level) is almost 3 orders longer than the lifetimes excited by 375 nm (ns level).

To investigate the light plasticity of the s-OOSTs, differnt light pulses with wavelengths ranging from UV (365 nm) to visible (blue: 465 nm, green: 520 nm, and red: 620 nm) to NIR (850/1050 nm) were used for regulating the PSC, which is the widest range of light response ever reported in the field of synapses. To investigated the influence of the light intensity on the synaptic behavior, white light with different intensity of 25, 50, 100 μW/cm$^2$ were used to stimulate the s-OOSTs. The ΔPSC increased with the increasing light intensity (Supplementary Fig. 13). The intensity of all kinds of light in the following test was fixed at 25 μW/cm$^2$. As shown in Supplementary Fig. 14, the energy consumption of different light wavelength ranges from 0.2 aJ ($\lambda = 1050$ nm) to 1.05 aJ ($\lambda = 365$ nm), which is lower than any other stretchable synaptic transistors reported before to the best of our knowledge (see Supplementary Table 2). In addition, the S/N and SNR value of them were obvious when stimulated by $V_D = -100$ μV with an ultra-low energy consumption, which are also included in Supplementary Table 3. The synaptic behaviors of the s-OOSTs under light pulse stimulation are shown in Fig. 4c–f. The ΔPSC increased as the light pulse width enlarged from 100 ms to 2000 ms, indicating that more pulse duration time of light can induce more carriers in the PTDPPSe-6Si channel. Meanwhile, the ΔPSC also increased with a decreasing wavelength of light, which is ascribed to the higher photon energy for the light with shorter wavelength[47]. Similar results were found for the s-OOSTs under 50% strain (Supplementary Fig. 15). The corresponding *ReC* and *MeC* for the s-OOSTs under light pulse stimulation are shown in Supplementary Fig. 16. Both *ReC* and *MeC* were regulated well by the pulse width and wavelength of the incident light even under 50% strain.

The relaxation time (defined by the time for the ΔPSC decreasing from peak to half after removing the light) also increased with an increasing pulse width of the incident light. For example, when the light pulse width increased from 100 ms to 2000 ms, the relaxation time increased from 1.37 s to 1.69 s (under the 1050 nm light). However, unlike ΔPSC, the relaxation time increased with an increasing wavelength of the incident light (Supplementary Fig. 17). For example, when the light wavelength increased from

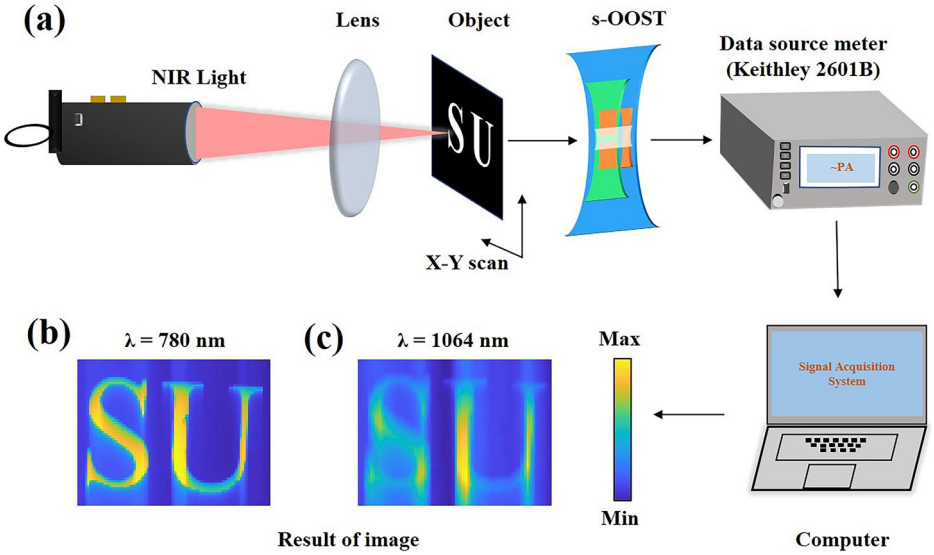


**Fig. 5 | NIR imaging of the s-OOSTs. a** Schematic illustration of the NIR imaging system using the s-OOSTs as the sensing pixel. **b** Image obtained from the 780 nm NIR imaging system. **c** Image obtained from the 1064 nm NIR imaging system.

365 nm to 1050 nm, the relaxation time increased greatly from 0.39 s to 1.69 s. This may be attributed to the long lifetime for the intramolecular charge transfer between donor and acceptor of the PTDPPSe-6Si under red/NIR light stimulation (compared to shorter reconbination time of $\pi - \pi^*$ transitions stimulated by UV light). According to the test of NIR/fluorescence lifetime in Supplementary Fig. 12, the longer lifetime of NIR light (excited by 808 nm) may lead to a longer memory effect (compared to the ns level lifetime of fluorescence (excited by 375 nm)). On the other hand, the excellent emission properties (according to the permanent $\Delta_0$,) and the different wavelength emission possibility (according to the permanent $\gamma$) fit by Eq. (9) lead to different resolution and recombination efficiency of excitons, and further result in different ΔPSC trendency. The results indicate that the light wavelength has a much greater impact on the relaxation time than the light pulse width. Figure 4d shows the ΔPSCs of the s-OOST stimulated by two successive light pulses with different wavelengths. And Supplementary Fig. 18 shows the ΔPSCs of the s-OOSTs stimulated by two successive light pulses with different $\Delta t$ (50–1000 ms), different wavelengths (365–1050 nm) and different strain states (0% and 50%). The corresponding PPF index under light stimulation are shown in Supplementary Fig. 19. The 850 nm NIR light stimulated devices had the highest PPF index (264%), while the 365 nm UV light stimulated devices had the lowest PPF index (137%). The higher PPF under 850 nm NIR light stimulation compared to those under other light stimulation is attributed to the strong absorption and long relaxation time in the 800–930 nm regime, which is originated from D-A intramolecular charge transfer the PTDPPSe-6Si. Upon stretching by 50%, the PPF index did not changed much. The results indicate that the s-OOSTs possesses highly reliable retina-inspired visual plasticity even under 50% strain.

In biological synapses or visual nerves, when the frequency of the presynaptic pulses changes, a synaptic weight change can be generated (SFDP). As the frequency increases, the ΔPSC increases. If the ΔPSC is larger than the threshold, the synapses or visual nerves will "fire" an action potential, which indicates high-pass filtering behavior (filtering characteristics). Here, 10 successive light pulses with a width of 50 ms and different frequencies (1.81, 3.33, 5.71, 10 and 13.33 Hz, corresponding to $\Delta t$ of 500, 250, 125, 50, 25 ms, respectively) were applied to the s-OOSTs to illustrate the high-pass filtering characteristics, as shown in Fig. 4e, f. The ΔPSCs increased clearly with an increasing frequency. If defining the ΔPSC at a frequency of 10 Hz as the threshold, the unstretched s-OOSTs "fired" an action potential when frequency was higher than 10 Hz. The ratios of the ΔPSCs at different frequency to that at 10 Hz are shown in Supplementary Fig. 20. When the s-OOSTs were stretched at 50%, the ΔPSCs also increased clearly with an increasing frequency, but the ΔPSCs were lower than those of unstretched s-OOSTs. This is mainly because the output current decreases as the applied strain increases. To investigate the heating effect of the s-OOSTs during the light stimulation, the infrared thermometer was used to take pictures after illuminating the device in the UV ($\lambda$ = 365 nm) and NIR light ($\lambda$ = 1050 nm) for 10 min (Supplementary Fig. 21). The heating effect is neglectable which may be due to the relatively low intensity of light. Supplementary Table 2 summarized the properties of the multi-wavelength responsive synapses reported before. To the best of our knowledge, our s-OOST has the widest wavelength response among all kinds of ever reported synaptic devices including the rigid[1,48–61] /bendable[3,6,7,9,10] /stretchable[8,15,17,18,62] ones, which indicates that the s-OOSTs have great potential to simulate the animal retinas that can sense the light from UV to NIR.

### Synaptic performance at low temperature

The s-OOSTs were further characterized at low temperature (from 293 K to 213 K with the step of –20 K, Supplementary Fig. 22). Under the same temperature condition, the ΔPSC (or *ReC*) decreased as the light wavelength increased. The *ReC* level in vacuum condition was quite lower than that in air condition, which might be attributed to the water (or oxygen) doping into the PTDPPSe-6Si channel. More interestingly, the ΔPSC (or *ReC*) response tendency in vacuum condition was also different from that in air environment. Under vacuum condition, when exposed to the light, the s-OOSTs exhibited a persistent *ReC* decay ($ReC_D$) over time (Supplementary Fig. 23), which might be attributed to the faster intramolecular charge transfer and faster carrier recombination under vacuum condition. Such behavior is similar to the self-adaptation process of the retina that automatically adjusts its sensitivity upon light irradiation (requiring a period of adaptation time before objects can be gradually seen). The visual self-adaptation properties of the s-OOSTs will be discussed in the following sections.

When the measuring temperature decreased, the ΔPSCs decreased. The conductance when light on ($G_{on}$) at different temperatures were calculated and depicted in Supplementary Fig. 24a. The decrease of $G_{on}$ (or *ReC*) with a decreasing temperature is due to the lower hopping possibility of the PTDPPSe-6Si at lower temperature. The thermally activated charge transport (Arrhenius plot) is expressed as[63]

$$G_{off} = A \exp\left(-\frac{E_a}{RT}\right) \quad (11)$$

where $R$ represents molar gas constant ($R$ = 8.314 J/(mol·K)), $E_a$ represents activation energy and $A$ is a proportional constant. The

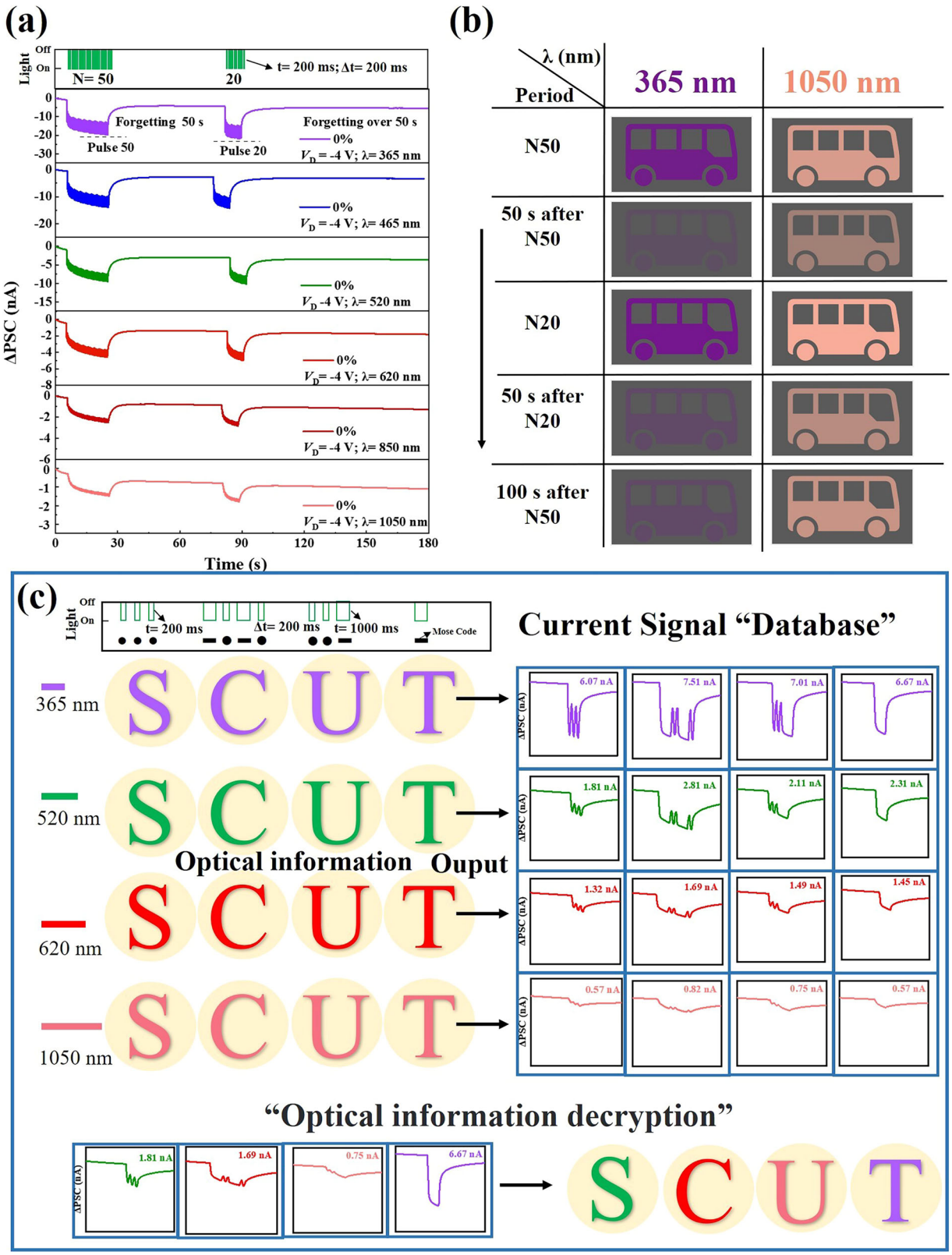


**Fig. 6 | Learning-forgetting-relearning" behavior under light stimulations and potential applications in artificial vision systems of the s-OOSTs. a** Learning-forgetting-relearning" behaviors under different light stimulations. **b** Simulated bus images under 365 nm and 1050 nm light, respectively, demonstrating distinct learning, forgetting and relearning behaviors. **c** The application of the Morse Code "encryption" and "decryption" of the s-OOSTs.

resulting $G_{off} \sim 1/T$ plot is shown in Supplementary Fig. 24b. A rough linearity of $G_{off}$ and $1/T$ was fitted with an $E_a$ of 0.35 eV. High $E_a$ means large amounts of grain boundaries or high inter-molecule transfer energy.

### Infrared imaging ability

To demonstrate the infrared imaging ability of the s-OOSTs, the image formation experiments were carried out using NIR sources integrated with s-OOST devices, as shown in Fig. 5a. Under the illumination of 780 nm and

1064 nm NIR light, the optical pattern projected on the a single-pixel imaging system was recognized by the s-OOST unit pixel. An imaging object with a photo mask of the letters "SU" was mounted on a stepping motor and controlled by a computer to move in the X-Y plane. When NIR light illuminated on the detector, the generated photocurrent can be collected by the backend circuit controlled by computer which was synchronized with the X-Y platform, forming a current value matrix. Then, the image of the object can be plotted by converting the data of photocurrent to the brightness of the image. As shown in Fig. 5b, c, a clear image of the letters "SU" with high contrast ratio was obtained for the device under 780 nm NIR light illumination, indicating high sensitivity of the s-OOST to the 780 nm NIR light. A less clear image of the letters "SU" with scanning traces was obtained for the device under 1064 nm NIR light illumination, which is attributed to the longer memory time under stimulation with longer-wavelength light of the s-OOST devices. The result shows that the s-OOSTs have the capability of the real-time broad-spectrum NIR imaging and can adapt to different light wavelengths.

### Self-adaptive image memory, polychromatic optical communication and security

The s-OOSTs can be used for image recognition and memory. The "learning-forgetting-relearning" behaviors under light (365-1050 nm) stimulation were performed by applying different periods of successive light pulses to the s-OOSTs. Figure 6a shows the levels of ΔPSC under "learning (50 successive pulses of light)-forgetting (removing the light for ~50 s)-relearning (20 successive pulses of light)" process with different wavelengths. After a period of learning by applying 50 successive pulses of light ($t$ = 200 ms, $\Delta t$ = 200 ms), the ΔPSC increased to 20.6 nA (365 nm), 14.73 nA (465 nm), 10.5 nA (520 nm), 5.54 nA (620 nm), 3.41 nA (850 nm) and 2.38 nA (1050 nm), respectively. After removing the light, the ΔPSC decreased and gradually stabilized. It reflects that the s-OOSTs have good memory ability for light signals. After the relearning period with much fewer pulses (20 successive pulses of light), the s-OOSTs reached a higher ΔPSC than that after the first period of learning strength, indicating that the s-OOSTs have certain associating and relearning ability under light regulations. Moreover, after the relearning period, the forgetting time increased to > 60 s. This indicates that the s-OOSTs can reduce the learning time and increase the memory time through training. As the wavelengths of the stimulating light increased, both of the ΔPSC and forgetting time increased, revealing that increasing the wavelength can reduce the learning time and enhance the memory ability. The similar learning results were found under 50% strain (Supplementary Fig. 25). Unlike the "Learning-forgetting-relearning" behavior under electrical pulse stimulation (Fig. 3a, b), which is caused by the slow ion migration in the ion-gel, the "learning-forgetting-relearning" behavior under light stimulation arises from the slow ICT process between donor and acceptor of the PTDPPSe-6Si semiconductor[45,64]. Therefore, the nonvolatility of the s-OOSTs under light pulse stimulation mainly depends on the ICT relaxation in the semiconductor itself.

The attenuations of the normalized ΔPSC in Fig. 6a were mapped to the changes of brightness of the images of a "bus". Firstly, the ΔPSC was normalized according to the maximum value of ΔPSC after triggered by 50 pulses of light, and the normalized ΔPSC was recorded to form the original "bus" image (Fig. 6b, N50). Then, the shapes of the "bus" image (ΔPSC) were recorded again after first period of 50 s forgetting (50 s after N50), relearning period of 20 pulses of light (N20), second period 50 s forgetting (50 s after N20) and 100 s forgetting (100 s after N20), respectively. For the 365 nm UV light stimulation, after first period of 50 s forgetting, the image became obscure. After 20 pulses of relearning, the image became clear again, even more clear than that after first N50 learning period. After second period of 50 s forgetting (50 s after N20), the image became obscure again, but more clear compared with that after the first forgetting period (50 s after N50). Prolonging the second period of forgetting time to 100 s, the image became a little more obscure, but could still be identified.

It is worth noting that the self-adaptive image learning and memory ability of the s-OOSTs under 1050 nm NIR light stimulation was much better than that under 365 nm UV light stimulation. After relearning period under 20 pulses of 1050 nm NIR light, the image became much more clear than that after first learning period of N50. And the image was still clear even after 100 s forgetting. The self-adaptive image learning and memory abilities of the s-OOSTs under light stimulation with other wavelength are shown in Supplementary Fig. 26a. The 850 nm NIR light stimulated devices had the best image learning and memory ability, while the 365 nm UV light stimulated devices had the poorest image learning and memory ability, which is in consistence with the above PPF results (originated from the D-A ICT process). Similar results can be found under 50% strain (Supplementary Fig. 26b). This phenomenon implies that the s-OOSTs may have the ability to indentify the wavelengths of light, which is of great significance for visual adaptive sensing of an object with different colors. To demonstrate the potential application of the s-OOSTs in optical information processing and optical communication, presynaptic light pulses representing Morse codes were employed to obtain the ΔPSC responses to English letters. During the test, the pulse widths of the short signal and long signal were set to 200 and 1000 ms, respectively. The pulse interval of the same letter is 200 ms. Figure 6c represents the ΔPSC responses of the unstretched s-OOSTs triggered by the Morse code of the letters "S", "C", "U" and "T" with light wavelength of 365 nm, 520 nm, 620 nm and 1050 nm, respectively. The ΔPSC responses of the 50% stretched s-OOSTs triggered by the Morse code of the letters is shown in Supplementary Fig. 27. Every letter displayed a distinct ΔPSC response under different-wavelength light pulse, even under 50% strain. Finally, a group of light message composed of different light wavelengths (colors) "S", "C", "U" and "T" was interpreted. Compared with the traditional photoelectronic synaptic transistors, the s-OOSTs have the wavelength identification ability (that is, "color" identification ability) that can further improve the "encryption" and "decryption" security for the optical communication. This property demonstrates that our s-OOSTs have great potential in applications polychromatic optical communication and optical information security for the stretchable artificial vision systems, and may eventually make a breakthrough in the next generation of intelligent neuromorphic sensing/computing-in-memory integrated systems.

## Discussion

In summary, a broadband (365–1050 nm) responsive s-OOST based on intrinsically stretchable, high-mobility, narrow-bandgap, high-relaxation-time organic semiconductor (PTDPPSe-6Si) was constructed to achieve brain-inspired memory/computation and retina-inspired visual perception/adaptation. The s-OOSTs exhibited high transconductance (86 mS) at a low voltage (−1 V) and could stand against 50% multidirectional strain. Its notable channel current brought high-density non-volatile multi-conductance states that were suitable for neuromorphic computation. Furthermore, the s-OOSTs can be stimulated by the light from ultraviolet (UV) to near-infrared (NIR) (365 nm–1050 nm), which is the widest wavelength response ever report. The relaxation time of the s-OOSTs changes greatly with the wavelengths of the incident light, making the devices possess additional abilities of light plasticity, color identification and visual self-adaptation similar to human retina. Moreover, synaptic performance was investigated at low temperature and vacuum condition. The broadband spectrum response makes it successfully image the letters "SU" in NIR environment with high contrast ratio in a single-pixel scanning imaging system, which verifies the feasibility for near-infrared sensing and visual response of the single s-OOST devices. Finally, multi-wavelength (365nm-1050 nm) optical synaptic plasticity was investigated for the imaging memory, polychromatic optical communication and information security. A series of "bus" images and letters (coded by wavelength) with different colors were identified and memorized by the s-OOSTs. The work paves a way for constructing an artificial system with dual modes of neuromorphic computation and visual perception, which are important for the next generation of intelligent sensing and computing-in-memory integrated systems.

## Methods

### Preparation of dextran sacrificial layer

The dextran solution was prepared by adding 1 mg dextran powder (Macklin, average $M_w$ 20,000) to 20 ml deionized water, then heating to 60 °C and stirring for 6 h. The thermoplastic polyurethane/dimethylformamide (TPU/DMF) solution was prepared by adding 1 mg TPU (Macklin, C80 A) to 4 mg DMF (Sigma-Aldrich, 98%) solution, then heating to 80 °C and stirring for 8 h. Firstly, the glass substrate was treated by oxygen plasma for 10 min to obtain a hydrophilic interface. The dextran solution was spin coated onto the substrate at a speed of 1000 rmp to form a 200 nm dextran film as a water-soluble sacrificial layer. Then, the TPU solution was scarped onto dextran film surface to form a 200 μm TPU film as a substrate.

### Preparation of ion-gel

**Material**. Acrylamide (AAm, 99%) and 2-Hydroxy-4'-(2-hydroxyethoxy)-2-methylpropiophenone (Irgacure 2959, 99%) were purchased from Shanghai Titan Scientific Co., Ltd. 2,2,2-Trifluoroethyl acrylate (TFEA, 98%) was purchased from Shanghai Qinba Chemical Co., Ltd., China. 1-Ethyl-3-methylimidazolium bis(trifluoromethylsulfonyl)imide ([EMIM][TFSI], 98%) was obtained from Monils Chemical (Shanghai) Co., Ltd., China.

**Fabrication**. The ion-gel was prepared by mixing 0.23 g AAm (Shanghai Titan Scientific Co., Ltd., 99% purity), 1.03 g TFEA (Shanghai Titan Scientific Co., Ltd., 98% purity), 1.89 g EMIM-TFSI (Monils Chemical (Shanghai) Co., Ltd., China) and 2 mg photoinitiator, and stirring thoroughly to obtain a uniform solution. Then pouring the solution onto the substrate, and irradiating it under an ultraviolet lamp for 2 h to obtain intrinsically stretchable ion-gel dielectric layer.

### Preparation of the s-OOSTs

Firstly, PTDPPSe-6Si was dissolved in chloroform (5 mg $mL^{-1}$) and was spin-coated on TPU substrates at 2000 rpm for 40 s. Then the polymer film was subsequently annealed at 100 °C for 30 min under nitrogen. The MWCNT was purchased from Xianfeng Nano Co., LTD., with a diameter of 20–40 nm, length > 5 μm, and a mass fraction of 10 wt.%. Then MWCNT film (150 nm) was patterned by spraying with MWCNT solution through a shading mask to form the source/drain electrodes and the side gate electrode. The channel width was 1000 μm and the length was 300 μm.

### Electrical and mechanical performance testing

The s-OSSTs were characterized using a semiconductor parameter analyzer (B1500A) and a pulse generator (DG4202). The stretching test was using a flexible-tensile machine. Light source was purchased from Taiyi Optoelectronics Co., Ltd.

## Data availability

The data that support the findings of this study are available from the corresponding author upon reasonable request.

## Code availability

All code for the analytic software is available from the corresponding author upon reasonable request.

Received: 11 September 2024; Accepted: 18 February 2025;
Published online: 02 March 2025

## References

1. Chen, K. et al. Organic optoelectronic synapse based on photon-modulated electrochemical doping. *Nat. Photonics* **17**, 629–637 (2023).
2. Zhang, J., Dai, S., Zhao, Y., Zhang, J. & Huang, J. Recent progress in photonic synapses for neuromorphic systems. *Adv. Intell. Syst.* **2**, 1900136 (2020).
3. Wang, X. et al. Enhanced multiwavelength response of flexible synaptic transistors for human sunburned skin simulation and neuromorphic computation. *Adv. Mater.* **35**, 2303699 (2023).
4. Wang, W. et al. Neuromorphic sensorimotor loop embodied by monolithically integrated, low-voltage, soft e-skin. *Science* **380**, 735–742 (2023).
5. Wang, S. et al. An organic electrochemical transistor for multi-modal sensing, memory and processing. *Nat Electron* **6**, 281–291 (2023).
6. Xu, Y. et al. Optically readable organic electrochemical synaptic transistors for neuromorphic photonic image processing. *Nano Letters* **23**, 5264–5271 (2023).
7. Zhang, J. et al. Bioinspired organic optoelectronic synaptic transistors based on cellulose nanopaper and natural chlorophyll-a for neuromorphic systems. *npj Flex Electron* **6**, 30 (2022).
8. Wang, C. et al. Strain-insensitive viscoelastic perovskite film for intrinsically stretchable neuromorphic vision-adaptive transistors. *Nat. Commun.* **15**, 3123 (2024).
9. Jiang, L. et al. Deep ultraviolet light stimulated synaptic transistors based on poly (3-hexylthiophene) ultrathin films. *ACS Appl. Mater. Interfaces* **14**, 11718–11726 (2022).
10. Zhang, J. et al. Retina-inspired artificial synapses with ultraviolet to near-infrared broadband responses for energy-efficient neuromorphic visual systems. *Adv. Funct. Mater.* **33**, 2302885 (2023).
11. Chen, H., Cai, Y., Han, Y. & Huang, H. Towards artificial visual sensory system: Organic optoelectronic synaptic materials and devices. *Angew. Chem. Int. Ed.* **63**, e202313634 (2024).
12. Molina-Lopez, F. et al. Inkjet-printed stretchable and low voltage synaptic transistor array. *Nat. Commun.* **10**, 2676 (2019).
13. Huang, B. et al. Skin-like n-type stretchable synaptic transistors with low energy consumption and highly reliable plasticity for brain-inspired computing. *Nano Energy* **128**, 109891 (2024).
14. Huang, W. et al. Intrinsically stretchable carbon nanotube synaptic transistors with associative learning ability and mechanical deformation response. *Carbon* **189**, 386–394 (2022).
15. Liu, L. et al. Stretchable neuromorphic transistor that combines multisensing and information processing for epidermal gesture recognition. *ACS nano* **16**, 2282–2291 (2022).
16. Shim, H. et al. Stretchable elastic synaptic transistors for neurologically integrated soft engineering systems. *Sci. Adv.* **5**, eaax4961 (2019).
17. Lee, Y. et al. Stretchable organic optoelectronic sensorimotor synapse. *Sci. Adv.* **4**, eaat7387 (2018).
18. Xie, T. et al. Carbon nanotube optoelectronic synapse transistor arrays with ultra-low power consumption for stretchable neuromorphic vision systems. *Adv. Funct. Mater.* **33**, 2303970 (2023).
19. Chen, J. et al. Highly stretchable organic electrochemical transistors with strain-resistant performance. *Nat. Mater.* **21**, 564–571 (2022).
20. Yang, Y. Ultraflexible, degradable organic synaptic Transistors based on natural polysaccharides for neuromorphic applications. *Adv. Funct. Mater.* **30**, 2006271 (2020).
21. Liu, L. et al. Functionalizing MXene towards highly stretchable, ultratough, fatigue- and fire-resistant polymer nanocomposites. *Chem. Eng. J.* **424**, 1385–8947 (2021).
22. He, Z. et al. Highly stretchable multi-walled carbon nanotube/thermoplastic polyurethane composite fibers for ultrasensitive, wearable strain sensors. *Nanoscale* **11**, 5884–5890 (2019).
23. Ding, Y. et al. Side chain engineering: Achieving stretch-induced molecular orientation and enhanced mobility in polymer semiconductors. *Chem. Mater.* **34**, 2696–2707 (2022).
24. Niu, Z. et al. Highly stretchable, integrated supercapacitors based on single-walled carbon nanotube films with continuous reticulate architecture. *Adv Mater* **25**, 1058–1064 (2013).
25. Xu, L. et al. A transparent, highly stretchable, solvent-resistant, recyclable multifunctional ionogel with underwater self-healing and

adhesion for reliable strain sensors. *Adv. Mater.* **33**, 2105306 (2021).
26. Yan, Y. et al. High-performance organic electrochemical transistors with nanoscale channel length and their application to artificial synapse. *ACS Appl. Mater. Interfaces* **12**, 49915–49925 (2020).
27. So, J. et al. Ionogel-gated organic transistors and artificial synapses based on a composite of tosylate-doped poly (3, 4-ethylenedioxythiophene) and insulating polyvinylpyrrolidone. *Macromol. Res.* **31**, 1095–1104 (2023).
28. Di Lauro, M. et al. Liquid-gated organic electronic devices based on high-performance solution-processed molecular semiconductor. *Adv. Electron. Mater.* **3**, 1700159 (2017).
29. Wang, N. et al. Ethylenedioxythiophene incorporated diketopyrrolopyrrole conjugated polymers for high-performance organic electrochemical transistors. *J. Mater. Chem. C* **9**, 4260–4266 (2021).
30. Ji, J. et al. Pulse electrochemical synaptic transistor for supersensitive and ultrafast biosensors. *InfoMat* **5**, 12478 (2023).
31. Zhu, H. et al. High-performance organic-inorganic hybrid thin-film transistors with interesting synaptic behaviors. *Phys. Status Solidi A* **216**, 1900344 (2019).
32. Han, S. et al. A high endurance, temperature-resilient, and robust organic electrochemical transistor for neuromorphic circuits. *J. Mater. Chem. C* **9**, 11801–11808 (2021).
33. Nguyen-Dang, T. et al. Biomaterial-based solid-electrolyte organic electrochemical transistors for electronic and neuromorphic applications. *Adv. Electron. Mater.* **7**, 2100519 (2021).
34. Deng, Y. et al. A flexible and biomimetic olfactory synapse with gasotransmitter-mediated plasticity. *Adv. Funct. Mater.* **33**, 2214139 (2023).
35. Li, X. et al. 3D-printed intrinsically stretchable organic electrochemical synaptic transistor array. *ACS Appl. Mater. Interfaces* **15**, 41656–41665 (2023).
36. Wang, W. et al. High-transconductance, highly elastic, durable and recyclable all-polymer electrochemical transistors with 3d micro-engineered interfaces. *Nano-Micro Lett* **14**, 184 (2022).
37. Fu, Y. M. et al. Electrolyte gated oxide pseudodiode for inhibitory synapse applications. *Adv. Electron. Mater.* **4**, 1800371 (2018).
38. Gao, W. T. et al. Dendrite integration mimicked on starch-based electrolyte-gated oxide dendrite transistors. *ACS Appl. Mater. Interfaces* **10**, 40008–40013 (2018).
39. Li, Y. et al. Ultrasensitive and degradable ultraflexible synaptic transistors based on natural pectin. *ACS Appl. Electron. Mater.* **4**, 316–325 (2021).
40. Mallik, S. K. et al. Ionotronic $WS_2$ memtransistors for 6-bit storage and neuromorphic adaptation at high temperature. *npj 2D Mater. Appl.* **7**, 63 (2023).
41. Dupuit, V. et al. A multifunctional hybrid graphene and microfluidic platform to interface topological neuron networks. *Adv. Funct. Mater.* **32**, 2207001 (2022).
42. Chen, J. et al. AlGaN/GaN MOS-HEMT enabled optoelectronic artificial synaptic devices for neuromorphic computing. *APL Mach. Learn.* **2**, 026113 (2024).
43. Kim, S. et al. Pattern Recognition Using Carbon Nanotube Synaptic Transistors with an Adjustable Weight Update Protocol. *ACS Nano* **11**, 2814–2822 (2017).
44. Dai, S. et al. Intrinsically stretchable neuromorphic devices for on-body processing of health data with artificial intelligence. *Matter* **5**, 3375–3390 (2022).
45. Chen, F. et al. Bio-inspired artificial perceptual devices for neuromorphic computing and gesture recognition. *Adv. Funct. Mater.* **33**, 2300266 (2023).
46. Hu, G. et al. ZnO micro/nanowire-based photonic synapse with piezo-phototronic modulation. *Nano Energy* **89**, 106282 (2021).
47. Zhu, C. et al. A Quinoxaline-Based D–A Copolymer Donor Achieving 17.62% Efficiency of Organic Solar Cells. *Adv. Mater.* **33**, 2100474 (2021).
48. Yang, R. et al. All-optically controlled artificial synapse based on full oxides for low-power visible neural network computing. *Adv. Funct. Mater.* **34**, 2312444 (2023).
49. Qiu, W. et al. Optoelectronic In-Ga-Zn-O memtransistors for artificial vision system. *Adv. Funct. Mater.* **30**, 2002325 (2020).
50. Mi, Y. C., Yang, C. H., Shih, L. C. & Chen, J. S. All-optical-controlled excitatory and inhibitory synaptic signaling through bipolar photoresponse of an oxide-based phototransistor. *Adv. Optical Mater.* **11**, 2300089 (2023).
51. Li, H. et al. Fully photon modulated heterostructure for neuromorphic computing. *Nano Energy* **65**, 104000 (2019).
52. Lu, C. et al. Self-rectifying all-optical modulated optoelectronic multistates memristor crossbar array for neuromorphic computing. *Nano Lett* **24**, 1667–1672 (2024).
53. Cheng, W. et al. Proton conductor gated synaptic transistor based on transparent igzo for realizing electrical and UV light stimulus. *IEEE J. Electron Devi.* **7**, 38–45 (2018).
54. Xiong, H. et al. Optically modulated hfs2-based synapses for artificial vision systems. *ACS Appl. Mater. Interfaces* **13**, 50132–50140 (2021).
55. Liu, J. et al. Weak light-stimulated synaptic hybrid phototransistors based on islandlike perovskite films prepared by spin coating. *ACS Appl. Mater. Interfaces* **13**, 13362–13371 (2021).
56. Yin, L. et al. Optically stimulated synaptic devices based on the hybrid structure of silicon nanomembrane and perovskite. *Nano Lett* **20**, 3378–3387 (2020).
57. Yang, C. M. et al. Bidirectional all-optical synapses based on a 2D $Bi_2O_2Se$/graphene hybrid structure for multifunctional optoelectronics. *Adv. Funct. Mater.* **30**, 2001598 (2020).
58. Islam, M. M., Dev, D., Krishnaprasad, A., Tetard, L. & Roy, T. Optoelectronic synapse using monolayer $MoS_2$ field effect transistors. *Sci. Rep.* **10**, 21870 (2020).
59. Liu, Z. et al. Photoresponsive transistors based on lead-free perovskite and carbon nanotubes. *Adv. Funct. Mater.* **30**, 1906335 (2020).
60. Zhang, J. et al. Tailoring neuroplasticity in flexible perovskite QDs-based optoelectronic synaptic transistors by dual modes modulation. *Nano Energy* **95**, 106987 (2022).
61. He, W. et al. A multi-input light-stimulated synaptic transistor for complex neuromorphic computing. *J. Mater. Chem. C* **7**, 12523–12531 (2019).
62. Li, J. et al. Highly stretchable $MoS_2$-based transistors with opto-synaptic functionalities. *Adv. Electron. Mater.* **8**, 2200238 (2022).
63. Li, S. Charge Transport in Blue Quantum Dot Light-Emitting Diodes. *Adv. Electron. Mater.* **10**, 2400142 (2024).
64. Wang, X. et al. Stretchable vertical organic transistors and their applications in neurologically systems. *Nano Energy* **90**, 106497 (2021).

## Acknowledgements

This work was supported in part by National Key R&D Program of China under Grant 2022YFB3603805, 2024YFF1504501 and 2021YFB3600800; in part by the National Natural Science Foundation of China under Grant 62474070 and 62074059; in part by the Project of High-Mobility High-Stability Oxide TFT Development and Applications under Grant 2024ZD0604100; in part by TCL science and technology innovation fund; and in part by the autonomous project of State Key Laboratory of Luminescent Materials and Devices under Grant Skllmd-2024-04.

## Author contributions

L.L. and B.H. designed the overall experiment. L.L. and B.H. conducted experiments and collected related data. B.H. and J.H. designed the image recognition simulation. L.L. and B.H. wrote the manuscript. Y.L., J.P., C.W., J.H., B.C., Q.Z., and Y.D. helped to performed the device simulation and analyses. L.Q., Q.W., Z.J., Y.L., J. P., and Y. C. revised the manuscript. All the

authors discussed the results and contributed to the manuscript preparation and have given their approval to the final version of the manuscript.

## Competing interests
The authors declare no competing interests.

## Additional information
**Supplementary information** The online version contains supplementary material available at https://doi.org/10.1038/s41528-025-00390-y.

**Correspondence** and requests for materials should be addressed to Linfeng Lan, Longzhen Qiu or Junbiao Peng.